Geophysical Research Letters

RESEARCH LETTER
10.1029/2019GL085120

Thermospheric Heating and Cooling Times During Geomagnetic Storms, Including Extreme Events

Eftyhia Zesta[1] and **Denny M. Oliveira**[1,2]

[1]Geospace Physics Laboratory, NASA Goddard Space Flight Center, Greenbelt, MD, USA, [2]Goddard Planetary Heliophysics Institute, University of Maryland, Baltimore County, Baltimore, MD, USA

Key Points:
- Thermosphere heating and cooling times are computed for geomagnetic storms with different intensities
- The most extreme storms heat and cool faster
- The fastest cooling effects are presumably caused by large amounts of nitric oxide produced during the most extreme events

Correspondence to:
E. Zesta,
eftyhia.zesta@nasa.gov

Citation:
Zesta, E., & Oliveira, D. M. (2019). Thermospheric heating and cooling times during geomagnetic storms, including extreme events. *Geophysical Research Letters*, *46*, 12,739–12,746. https://doi.org/10.1029/2019GL085120

Received 22 AUG 2019
Accepted 3 NOV 2019
Accepted article online 11 NOV 2019
Published online 29 NOV 2019

Abstract We present the first quantitative calculations of thermospheric heating and cooling times for geomagnetic storms of different intensity, including extreme events. We utilize the neutral mass density database of the CHAllenging Mini-satellite Payload and Gravity Recovery And Climate Experiment missions to produce thermospheric global system response to geomagnetic storms caused by coronal mass ejections via superposed epoch analysis during May 2001 to December 2015. Storm events are grouped in five different categories based on the minimum value of the SYM-H index. We calculate the time from storm onset for the thermosphere to reach maximum intensification (heating time) and the time from onset for the thermosphere to recover (cooling time). We find that heating and cooling times decrease as storm intensity increases and the effect is more pronounced for the cooling times. For extreme storms, the thermospheric heating time is 9.5 hr, while the cooling time is 22 hr.

1. Introduction

The Earth's thermosphere density, temperature, and structure are driven by the Sun's variable energy. While solar extreme ultraviolet radiation is generally the major thermospheric driver, during geomagnetic storms, magnetospheric energy input is the dominant driver of thermospheric heating (Knipp et al., 2004; Prölss, 2011). Magnetospheric energy is deposited in the Earth's high-latitude regions first and quickly moves equatorward to all latitudes (Lu et al., 2016). The whole thermosphere circulates, heats up, and rises.

Satellites at low-Earth orbit fly within the thermosphere and are continuously impacted by its molecules increasing the friction the satellite experiences along its orbit. Under nonstorm conditions, this "orbital drag" impacts satellites below 500 km altitudes. The International Space Station has to routinely correct its orbit due to drag effects. During geomagnetic storms, however, all low-Earth orbit satellites, even higher than 600 km, find themselves within a denser atmosphere, experiencing orbital altitude decay and potential loss of tracking knowledge (e.g., Oliveira & Zesta, 2019; Zesta & Huang, 2016).

The severity of such effects depends on the strength of the storm. Existing models can reproduce the drivers and thermospheric responses in general terms but cannot yet reproduce and predict their timing, structure, or intensity. There are two difficulties. Existing empirical models, like the Jacchia (1970, 1977) and Mass Spectrometer and Incoherent Scatter radar (Hedin, 1987; Picone et al., 2002) family models or the Jacchia-Bowman model (Bowman et al., 2008, henceforth JB08), typically characterize the thermosphere by a single exospheric temperature T_∞, thus missing the circulation, waves, and mesoscale structure along the path of individual satellites (Fuller-Rowell et al., 1994). Physics-based models, on the other hand, are starved for realistic energy inputs of ionospheric potential patterns and precipitating particles (Connor et al., 2016; Verkhoglyadova et al., 2007). More important, thermosphere's response to increasing energy input is not linear; there are saturation effects, which we do not understand.

Ngwira et al. (2014) attempted a global magnetohydrodynamic simulation of a Carrington-type event using the Space Weather Modeling Framework (Tóth et al., 2005). Their results showed the magnetopause standoff distance at 2 R_E, cross polar cap potential of 2,000 kV, and the polar cap extending down to 20° geomagnetic latitude. Such responses would have dangerous and detrimental impacts on humanity, but saturation effects and internal self-regulating mechanisms are not included in current models.

Recent works have pointed out that the thermosphere recovers after a strong storm faster than predicted by models. Lei et al. (2011) found from CHAllenging Mini-satellite Payload (CHAMP) and Gravity Recovery And Climate Experiment (GRACE) observations that the observed recover time of the thermosphere

during the 2003 Halloween storms was significantly shorter than predicted by either the empirical Mass Spectrometer and Incoherent Scatter radar model or the Thermosphere Ionosphere Electrodynamics General Circulation Model physics-based model. Knipp et al. (2017) demonstrated that for shock-led coronal mass ejections (CME) storms, nitric oxide (NO), production occurs "early and excessively," which leads to the much faster recovery of these storms, as NO is a significant radiative cooling agent for the thermosphere (e.g., Mlynczak et al., 2003).

Here we use density as a proxy for thermospheric temperature, which is the premise of both global hydrostatic models (e.g., Kodikara et al., 2019) and empirical models (Jacchia, 1970, 1977). While Lei et al. (2010) found that both winds and composition impact the density in addition to temperature, our assumption is appropriate for system-level approach.

We follow the analysis methodology performed in Oliveira et al. (2017), who provided global thermospheric density responses to geomagnetic storms through a superposed epoch analysis of CHAMP and GRACE satellite observations for a large number of storms. We provide the same superposed epoch density dynamics but for storms of different strengths and quantitatively determine, on a system level, the heating and cooling times of the thermosphere with a particular emphasis on extreme storms.

2. Data Sources

For storm identification, we use the CME catalog of Richardson and Cane (2010) (http://www.srl.caltech.edu/ACE/ASC/DATA/level3/icmetable2.htm#(a)). We identified a total of 217 storms during the period from May 2001 to December 2015.

We use accelerometer data from the CHAMP (Reigber et al., 2002) and GRACE (Tapley et al., 2004) satellite missions to determine thermospheric density during storms. CHAMP data are obtained through https://isdc.gfz-potsdam.de/champ-isdc/access-to-the-champ-data/ and GRACE data through https://isdc.gfz-potsdam.de/grace-isdc/grace-gravity-data-and-documentation/ at the website of the Information System and Data Center in Postdam, Germany.

The CHAMP and GRACE densities are normalized and intercalibrated as was discussed in Oliveira et al. (2017). We use the JB08 model as common baseline and follow the outlined approach:

1. For each satellite, we isolate all periods within their database with low geomagnetic activity (LGA), defined when|SYM-H|< 30 nT, which constitute the majority of each satellite's database. For these periods, we calculate the ratio ρ_{obs}/ρ_{LGA}, where ρ_{obs} is the observed density and ρ_{LGA} is the JB08 density calculated for the interval conditions. This step normalizes the satellite measured density against the JB08 model similarly for both satellites during quiet conditions.
2. We fit the ρ_{obs}/ρ_{LGA} ratio for the entirety of the LGA intervals within each satellite's database with a 15-degree polynomial function (Arlinghaus, 1994) to produce the calibration function f(t) as a function of time and at the satellite altitude (see Oliveira et al., 2017, and their Figure 1 for a depiction of this process). The function f(t) is then interpolated to cover all data, including the storm periods in our study. This step provides the calibration functions $f_{CH}(t)$ and $f_{GR}(t)$ for the two satellites.
3. We wish to isolate the effect of storms on the neutral density, so we use the JB08 model with input Dst = 0 to provide the nonstorm quiet time reference densities. For each storm, we calculate the model quiet density at the satellite's altitude as $\rho_0(t) = \rho_{JB08}(t,Dst = 0)$. Then the cross-calibrated quiet time densities are

$$\rho_{0,CH}(t) = \rho_0(t)\, f_{CH}(t) \quad \text{and} \quad \rho_{0,GR}(t) = \rho_0(t)\, f_{GR}(t). \tag{1}$$

4. For our analysis, we use the density ratios of $\rho_{CH}(t)/(f_{CH}(t)\rho_0(t))$ and $\rho_{GR}(t)/(f_{GR}(t)\rho_0(t))$ that have observed densities normalized against the quiet density. This approach assures that these ratios are close to 1 during quiet times and much larger during storm times. These are the density ratios that are cross-calibrated between the two satellites and can be plotted together.

The 1-min solar wind plasma and interplanetary magnetic field (IMF) observations are taken from the OMNIWeb site (http://omniweb.gsfc.nasa.gov).

Table 1
Storm Classification

Type of storm event	SYM-H limits (nT)	Number of events
Weak	$-50 <$ SYM-H	90
Moderate	$-100 <$ SYM-H < -50	78
Strong	$-150 <$ SYM-H < -100	28
Severe	$-250 <$ SYM-H < -150	14
Extreme	SYM-H < -250	7
Total storms		217

The geomagnetic activity index SYM-H is from the World Data Center in Kyoto, Japan, website (http://wdc.kugi.kyoto-u.ac.jp/aeasy/index.html). The SYM-H index is similar to the Dst index but with 1-min resolution (Iyemori, 1990; Katus & Liemohn, 2013).

3. Storm Classification

The Space Weather Action Plan was released from the Office for the Science and Technology for the President in 2015, and it identified extreme events as "one in 100 years" type of events, in nomenclature similar to that used for extreme tropospheric weather (National Science and Technology Council, 2015). However, the Dst index is produced continuously only since 1957. Reliance of human life on space assets is significantly shorter, no more than 40 years. There is no objective, or generally accepted, way to determine the "one in 100 years" event (Riley et al., 2018). The strongest horizontal geomagnetic field perturbations of approximately −1,700 nT occurred during the Carrington event of September 1859 (Tsurutani et al., 2003; Hayakawa et al., 2019), and the most intense storm in the post-Dst era occurred in March 1989, Dst = −589 nT (Allen et al., 1989).

We characterize different storms as *weak*, *moderate*, *strong*, *severe*, and *extreme*, based on the magnitude of the SYM-H index and based on our experience in analyzing hundreds of storms. We also choose the SYM-H over the Dst index because the Dst index, being a 1-hr index averages over the true minima of the storm that are better quantified by the 1-min cadence of the SYM-H index. Table 1 summarizes the SYM-H limits for each storm category, as well as the number of storms in each category during the studied period. The two strongest categories have the smallest number of storms. For severe storms, we excluded from our list two storms that had a second storm occurring during their recovery because when included they bias the overall heating and cooling trends.

Table 2 is a list of the seven extreme storms that occurred in the time period of this study, that is, during the CHAMP and GRACE era, along with the basic characteristics of the storms. These are all CME-driven storms. We define storm onset time as the onset of the southward IMF B_z turning. Extreme storms are extremely rare, and only 39 events occurred since 1957 with minimum Dst ≤ -250 nT (Meng et al., 2019).

4. Results

Figure 1 shows CHAMP and GRACE density responses during the extreme storm of 20 November 2003. From top to bottom are the SYM-H index, the B_y (cyan) and B_z (magenta) components of the IMF, the time series of the CHAMP density, the CHAMP density with respect to magnetic latitude (MLAT) and universal time (UT), the GRACE density time series, and the GRACE density with respect to MLAT and UT. In the latitudinal density plots, densities are binned by 5° in MLAT. CHAMP and GRACE are both in a near noon-midnight meridian with CHAMP orbit ascending node on the dayside and GRACE orbit ascending node on the nightside.

The first vertical dashed line identifies the pre-CME shock impact, and the second vertical line identifies the storm onset. Density enhancements are observed first at high latitudes for both satellites. The intensifications are stronger after the storm onset and they quickly (within two to three orbits) propagate to the equator and the nightside. Nine hours after the storm onset, at 2024 UT on 20 November, the enhanced density starts decreasing, and within 24 hr from onset, it is back at the prestorm levels.

Table 2
The List of the Seven Extreme Storms

Storm #	Date	Onset UT	Min IMF-B_z (nT)	Min SYM-H (nT)
1	6 Nov 2001	02:05	−78.97	−320
2	29 Oct 2003	07:04	−62.09	−390
3	30 Oct 2003	20:13	−35.99	−432
4	20 Nov 2003	11:24	−52.97	−490
5	7 Nov 2004	20:14	−50.49	−394
6	9 Nov 2004	19:25	−34.14	−282
7	15 May 2005	06:01	−46.58	−305

We statistically demonstrate that the fast recovery of the neutral density to its prestorm levels is a persistent characteristic of severe and extreme storms.

Figure 2 shows superposed epoch latitudinal distribution of the neutral mass density during the different strength storms as identified in Table 1 and in panels b–f, respectively. Figure 2a shows the superposed epoch distribution of all storm types together, and it is similar to Figure

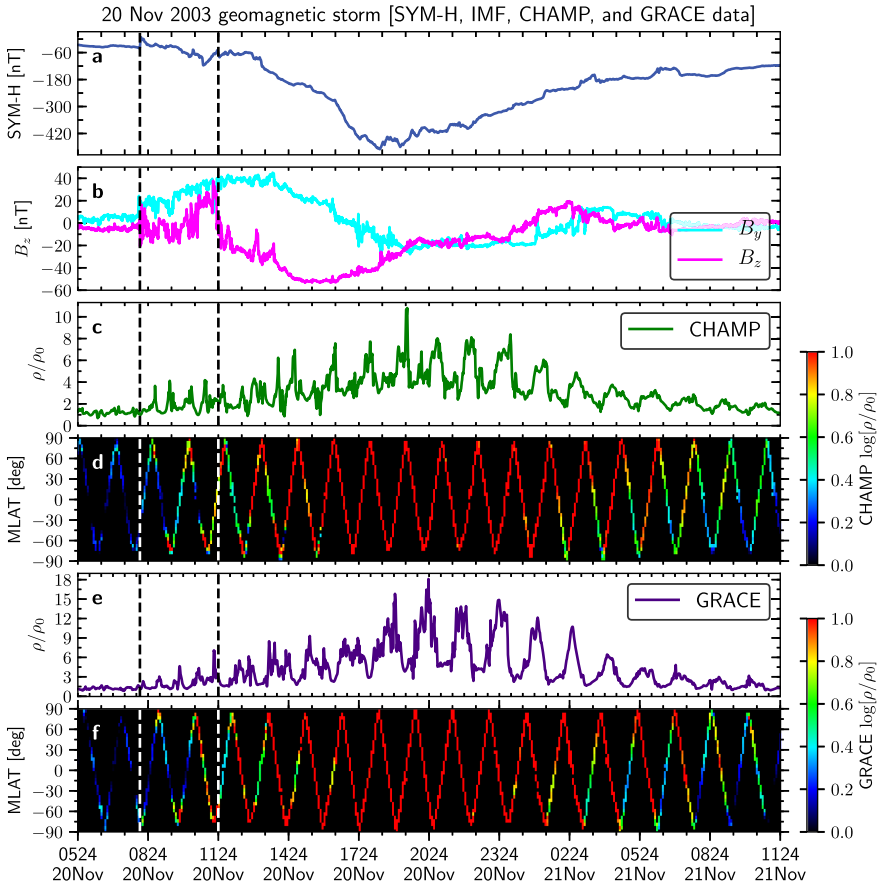

Figure 1. Extreme storm event of 20 November 2003. A period of 30 hr is shown around the event. The time period plotted is from 20 November 0524 UT to 21 November 1124 UT. From top to bottom are (a) the storm activity SYM-H index, (b) the IMF Bz and By components, (c) the time series of the CHAMP normalized neutral density, (d) the CHAMP neutral density versus UT and magnetic latitude, (e) the GRACE time series of the GRACE normalized neutral density, and (f) the GRACE neutral density versus UT and magnetic latitude.

8(d) in Oliveira et al. (2017) but with a larger number of storms. Epoch time includes 12 hr before storm onset and 72 hr after storm onset.

Similar to Oliveira et al. (2017), we bin by 3° in MLAT and 15 min in UT. The density for all storm types is plotted in the same color table range, to facilitate direct comparison. The quantity plotted in Figure 2 is the logarithm of the density ratio in equation (1).

For all storm strengths, the high latitudes respond almost immediately (to within the 15 min of the time bin). For weak storms, the intensification remains at high latitudes, and only weak intensifications are seen to propagate equatorward. For moderate, strong, severe, and extreme storms, the range of high latitudes that respond immediately after the storm onset progressively increases, the time it takes for the high-latitude intensification to propagate to the equator decreases, and the time it takes the density to recover significantly decreases with storm strength. For the extreme events (panel f), density intensifications reach the equator only 1.5 hr after storm onset, a time much shorter than the 3.0 hr that was found in Oliveira et al. (2017).

From the latitudinal density distribution development over epoch time during different storm strengths in Figure 2, we can quantify the thermospheric heating and cooling times for the different types of storms. The reference time for both heating and cooling times is the storm onset, epoch time 0 hr. As studies noted before (e.g., Knipp et al., 2017; Lei et al., 2011; Mlynczak et al., 2018), Joule heating and particle precipitation sharply increase at storm onset and heat the thermosphere while, at the same time, also contribute to NO production, which immediately begins to radiatively cool the thermosphere. The heating and cooling processes operate together, and it is the balance of the two that is the measure of the temperature, and by proxy the

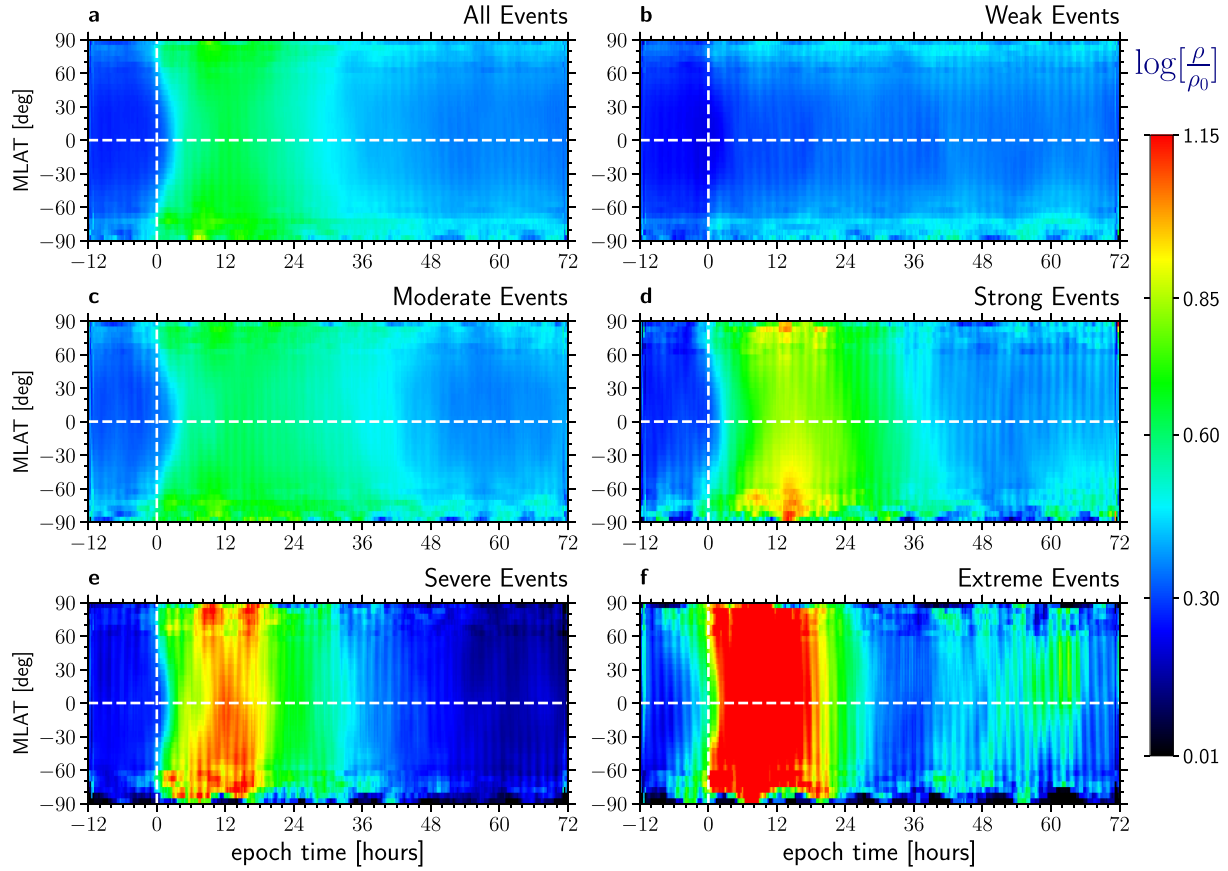

Figure 2. Superposed epoch analysis of the density latitudinal distribution with epoch time during the five types of storm strength. The property plotted is the cross-calibrated density from the two satellites (CHAMP and GRACE) normalized by the nonstorm quiet density. Note that weaker density enhancements seen before the storm onset, primarily at high latitudes in (a)–(e) and in a wider range of latitudes in (f), are the result of the CME shock impact and the CME sheath activity that impact the magnetosphere before the storm onset (e.g., Shi et al., 2017).

density, at each moment through the storm. We thus define as "heating time" the time from onset it takes for the density to reach its peak value and as "cooling time" the time from onset it takes for the density to cycle through its peak and return to 25% of its prestorm value. The assumption is that the heating and cooling of the thermosphere increase and decrease the density at a given altitude by raising and bringing down the neutral gas, respectively. We acknowledge that circulation of the gas by horizontal winds is also folded into the observed density changes, but at the system level, the temperature is the primary driver.

To quantify the heating and cooling times, we isolate the density at middle and low latitudes, from −50° to +50° MLAT, and calculate the average over this latitude range at every 15-min time bin. A Savitzky-Golay filter applied to Weibul distribution fits of the density averages was used to smooth the averaged data, as described by Oliveira et al. (2017). Figure 3 shows the middle and low latitude average density curves for weak to extreme storms stacked from top to bottom. Error bars are plotted along the curves every 6 hr. The black dashed line indicates storm onset. The red dashed lines indicate the time, t_{max}, when the density reaches its maximum value, and it is calculated by the zero crossing of the first derivative of the density curve. The blue dashed line identifies the time, $t_{25\%}$, when the average density reaches the 25% of its maximum value. The 25th percentile reduction is ~10% more than the *e*-folding time of the curve, and we use it as the quantifiable cooling time. The cooling times have a very clear progression to shorter ranges as the storm strength increases. Note that the prestorm and at-onset error bars are the largest ones for all categories due to the variable duration and activity of each CME sheath and its shock impact (see also Figure 2).

Figure 4 summarizes the heating and cooling times with respect to storm strength. The heating time has a severe drop between weak and moderate storms, remains level for moderate, strong, and severe storms,

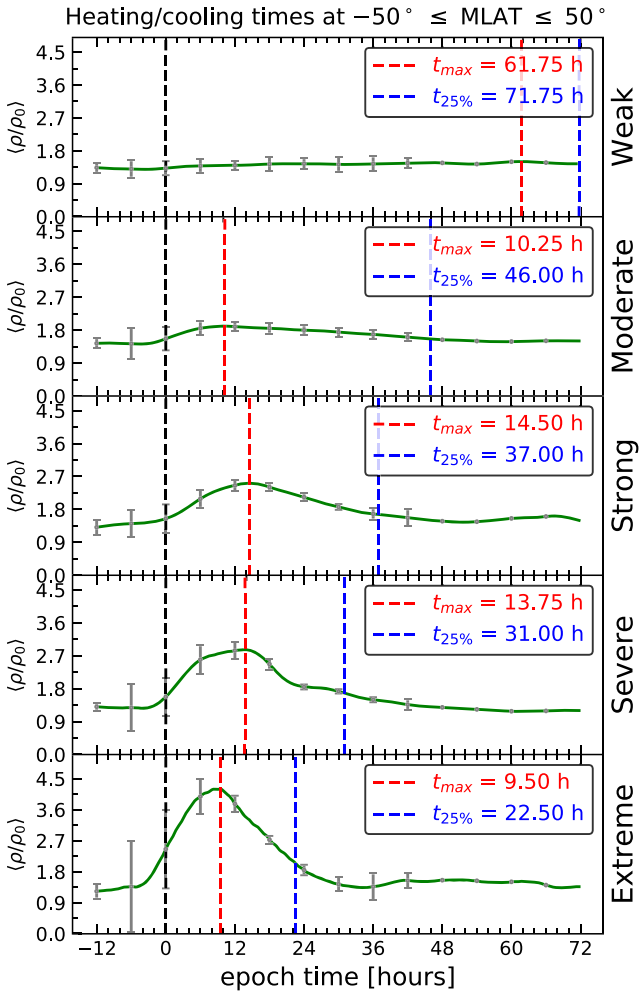

Figure 3. Middle and low latitude density curves with respect to epoch time through the storm for the five storm strengths. In each panel, the time from onset when the density reaches its maximum value is identified as t_{max} and the time from onset when the density recovers back to 25% of peak value, t_{25}% are indicated with the second and third vertical dashed lines, respectively. The first vertical line indicates the storm onset. The t_{max} and t_{25}% times are noted within a box for each storm type. A Savitzky-Golay filter applied to Weibul distributions was used to filter the averaged density data (Oliveira et al., 2017). Error bars, signifying the 1 standard deviation, are plotted every 6 hr along the curves. The size of the error bars is generally smaller than the curve trend, demonstrating the statistical significance of the results.

and markedly drops for extreme events. The cooling time curve has a smooth, asymptotic decrease, consistent with the idea that heating during the storm depends on external drivers and energy inputs, while cooling depends on internal processes that regulate the behavior in an almost predictable fashion (Knipp et al., 2017; Mlynczak et al., 2003; Zhang et al., 2019).

Our result is consistent with the results with prior studies (Aguado et al., 2010; Lei et al., 2011) and with Knipp et al. (2017) although we find that the strength of the storm, rather than the existence of a shock dominate the faster cooling of the thermosphere.

Our results are in agreement with the Knipp et al. (2017) suggestion that it is NO overproduction during storms that leads to the faster recovery of the thermosphere because of its ability to radiatively cool the upper atmosphere. The density of NO is strongly controlled by auroral precipitation and Joule heating (Lu et al., 2010; Mlynczak et al., 2008), both of which are strong energy inputs during storms. NO created at high latitudes during geomagnetic storms can spread out to lower latitudes due to its long lifetime (Barth et al., 2009; Siskind et al., 1989), facilitating radiative cooling of lower latitudes, as we observe. We suggest that NO production is progressively stronger the stronger the storm. For stronger storms, the horizontal winds are stronger as well and can quickly transport NO to equatorial and mid latitudes where it regulates the cooling times

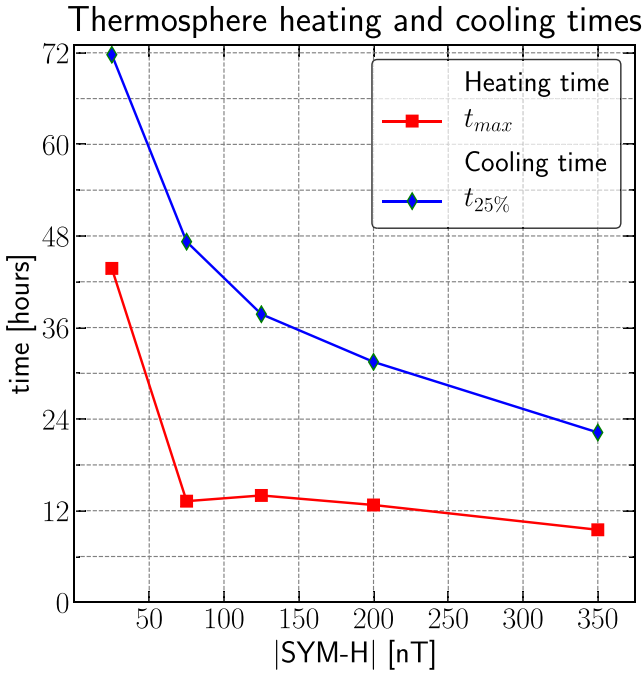

Figure 4. The storm heating and cooling times with respect to storm strength as described by the|SYM-H|index. The red line is the heating time curve, and the blue line is the cooling time curve.

of the thermosphere during storm recovery. The more NO that a storm produces at high latitudes from magnetospheric energy input, the faster the thermosphere cools. For extreme storms, we find that it takes only 1.5 hr from the storm onset for the density intensifications to reach the equator, 9.5 hr from onset for the thermosphere to reach its maximum density, and 22 hr from onset for the thermosphere to recover.

5. Summary

In this study, we investigated the effects of geomagnetic storms caused by CMEs on the dynamic thermosphere response. We provide, for the first time, quantitative heating and cooling times for the thermosphere for storms of different strengths. We utilized the full CHAMP and GRACE neutral mass density database to produce the superposed epoch latitudinal distributions of mass density during five different storm categories ranging from weak to extreme events. We found that the more intense the storm, the shorter the heating and cooling times. We also found that the most extreme storms presented the fastest heating and cooling times, reaching maximum intensification within 9.5 hr of onset and global cooling occurring at all latitude regions nearly simultaneously within 22 hr of onset. We attributed such cooling effects to high production of NO molecules that in turn play a major role in cooling the thermosphere.

Acknowledgments
The authors were supported for this work by NASA Grant NNH13ZDA001N-HSR and by the NASA Heliophysics Internal Scientist Funding Model (HISFM18-0009, HISFM18-HIF). We thank the GSFC/SPDF OMNI team for solar wind and IMF data availability. We thank Ian Richardson and Hillary Cane for their CME list compilation. All data used in this investigation are available online and the websites are provided in the second section of this manuscript.

References

Aguado, J., Cid, C., Saiz, E., & Cerrato, Y. (2010). Hyperbolic decay of the Dst index during the recovery phase of intense geomagnetic storms. *Journal of Geophysical Research*, *115*, A07220. https://doi.org/10.1029/2009JA014658

Allen, J., Sauer, H., Frank, L., & Reiff, P. (1989). Effects of the March 1989 solar activity. *Eos, Transactions American Geophysical Union*, *70*(46), 1479–1488. https://doi.org/10.1029/89EO00409

Arlinghaus, S. L. (Ed.) (1994). *Practical handbook of curve fitting*. Boca Raton, FL: CRC Press.

Barth, C. A., Lu, G., & Roble, R. G. (2009). Joule heating and nitric oxide in the thermosphere. *Journal of Geophysical Research*, *114*, A05301. https://doi.org/10.1029/2008JA013765

Bowman, B. R., Tobiska, W. K., Marcos, F. A., Huang, C. Y., Lin, C. S., & Burke, W. J. (2008). A new empirical thermospheric density model JB2008 using new solar and geomagnetic indices. In *AIAA/AAS Astrodynamics Specialist Conference* (Vol. 2008–6438, pp. 1–19). Honolulu, HI: AIAA.

Connor, H. K., Zesta, E., Fedrizzi, M., Shi, Y., Raeder, J., Codrescu, M. V., & Fuller-Rowell, T. J. (2016). Modeling the ionosphere-thermosphere response to a geomagnetic storm using physics-based magnetospheric energy input: OpenGGCM- CTIM results. *Journal of Space Weather and Space Climate*, *6*, A25. https://doi.org/10.1051/swsc/2016019

Fuller-Rowell, T. J., Codrescu, M. V., Moffett, R. J., & Quegan, S. (1994). Response of the thermosphere and ionosphere to geomagnetic storms. *Journal of Geophysical Research*, *99*(A3), 3893–3914. https://doi.org/10.1029/93JA02015

Hayakawa, H., Ebihara, Y., Willis, D. M., Toriumi, S., Iju, T., Hattori, K., et al. (2019). Temporal and Spatial Evolutions of a Large Sunspot Group and Great Auroral Storms around the Carrington Event in 1859. *Space Weather*, *17*. https://doi.org/10.1029/2019SW002269

Hedin, A. E. (1987). MSIS-86 thermospheric model. *Journal of Geophysical Research*, *92*(A5), 4649–4662. https://doi.org/10.1029/JA092iA05p04649

Iyemori, T. (1990). Storm-time magnetospheric currents inferred from mid-latitude geomagnetic field variations. *Journal of Geomagnetism and Geoelectricity*, *42*(11), 1249–1265. https://doi.org/10.5636/jgg.42.12

Jacchia, L. G. (1970). New static models of the thermosphere and exosphere with empirical temperature profiles, SAO Special Report 313.

Jacchia, L. G. (1977). Thermospheric temperature, density and composition: A new model, SAO Special Report 375.

Katus, R. M., & Liemohn, M. W. (2013). Similarities and differences in low- to middle-latitude geomagnetic indices. *Journal of Geophysical Research: Space Physics*, *118*, 5149–5156. https://doi.org/10.1002/jgra.50501

Knipp, D., Tobiska, W., & Emery, B. (2004). Direct and indirect thermospheric heating sources for solar cycles 21–23. *Solar Physics*, *224*, 495–505. https://doi.org/10.1007/s11207-005-6393-4

Knipp, D. J., Pette, D. V., Kilcommons, L. M., Isaacs, T. L., Cruz, A. A., Mlynczak, M. G., et al. (2017). Thermospheric nitric oxide response to shock-led storms. *Space Weather*, *15*, 325–342. https://doi.org/10.1002/2016SW001567

Kodikara, T., Carter, B., Norman, R., & Zhang, K. (2019). Density-temperature synchrony in the hydrostatic thermosphere. *Journal of Geophysical Research: Space Physics*, *124*, 674–699. https://doi.org/10.1029/2018JA025973

Lei, J., Thayer, J. P., Burns, A. G., Lu, G., & Deng, Y. (2010). Wind and temperature effects on thermosphere mass density response to the November 2004 geomagnetic storm. *Journal of Geophysical Research*, *115*. https://doi.org/10.1029/2009JA014754

Lei, J., Thayer, J. P., Lu, G., Burns, A. G., Wang, W., Sutton, E. K., & Emery, B. A. (2011). Rapid recovery of thermosphere density during the October 2003 geomagnetic storms. *Journal of Geophysical Research*, *116*, A03306. https://doi.org/10.1029/2010JA016164

Lu, G., Mlynczak, M. G., Hunt, L. A., Woods, T. N., & Roble, R. G. (2010). On the relationship of joule heating and nitric oxide radiative cooling in the thermosphere. *Journal of Geophysical Research*, *115*. https://doi.org/10.1029/2009JA014662

Lu, G., Richmond, A. D., Lühr, H., & Paxton, L. (2016). High-latitude energy input and its impact on the thermosphere. *Journal of Geophysical Research: Space Physics*, *121*, 7108–7124. https://doi.org/10.1002/2015JA022294

Meng, X., Tsurutani, B. T., & Mannucci, A. J. (2019). The Solar and Inter-planetary Causes of Superstorms (Minimum Dst ≤ −250 nT) During the Space Age. *Journal of Geophysical Research: Space Physics*, *124*, 3926–3948. https://doi.org/10.1029/2018JA026425

Mlynczak, M. G., Knipp, D. J., Hunt, L. A., Gaebler, J., Matsuo, T., Kilcommons, L. M., & Young, C. L. (2018). Space-based sentinels for measurement of infrared cooling in the thermosphere for space weather nowcasting and forecasting. *Space Weather*, *16*, 363–375. https://doi.org/10.1002/2017SW001757

Mlynczak, M. G., Martin-Torres, F. J., Mertens, C. J., Marshall, B. T., Thompson, R. E., Kozyra, J. U., et al. (2008). Solar-terrestrial coupling evidenced by periodic behavior in geomagnetic indexes and the infrared energy budget of the thermosphere. *Geophysical Research Letters*, *35*, L05808. https://doi.org/10.1029/2007GL032620

Mlynczak, M. G., Martin-Torres, F. J., Russell, J., Beaumont, K., Jacobson, S., Kozyra, J., et al. (2003). The natural thermostat of nitric oxide emission at 5.3 μm in the thermosphere observed during the solar storms of April 2002. *Geophysical Research Letters*, *30*(21), 2100. https://doi.org/10.1029/2003GL017693

National Science and Technology Council. (2015). National Space Weather Action Plan (Tech. Rep.). Washington, DC: Executive Office of the President of the United States. Retrieved from https://obamawhitehouse.archives.gov/sites/default/files/microsites/ostp/final nationalspaceweatheractionplan 20151028.pdf

Ngwira, C. M., Pulkkinen, A., Kuznetsova, M. M., & Glocer, A. (2014). Modeling extreme "Carrington-type" space weather events using three-dimensional global MHD simulations. *Journal of Geophysical Research: Space Physics*, *119*, 4456–4474. https://doi.org/10.1002/2013JA019661

Oliveira, D. M., & Zesta, E. (2019). Satellite orbital drag during magnetic storms. *Space Weather*, *17*. https://doi.org/10.1029/2019SW002287

Oliveira, D. M., Zesta, E., Schuck, P. W., & Sutton, E. K. (2017). Thermosphere global time response to geomagnetic storms caused by coronal mass ejections. *Journal of Geophysical Research: Space Physics*, *122*, 10,762–10,782. https://doi.org/10.1002/2017JA024006

Picone, J. M., Hedin, A. E., Drob, D. P., & Aikin, A. C. (2002). NRLMSISE-00 empirical model of the atmosphere: Statistical comparisons and scientific issues. *Journal of Geophysical Research*, *107*(A12), 1–16. https://doi.org/10.1029/2002JA009430

Prölss, G. (2011). Density perturbations in the upper atmosphere caused by the dissipation of solar wind energy. *Surveys in Geophysics*, *32*(2), 101–195. https://doi.org/10.1007/s10712-010-9104-0

Reigber, C., Lühr, H., & Schwintzer, P. (2002). CHAMP mission status. *Advances in Space Research*, *30*(2), 129–134. https://doi.org/10.1016/S0273-1177(02)00276-4

Richardson, I. G., & Cane, H. V. (2010). Interplanetary circumstances of quasi-perpendicular interplanetary shocks in 1996-2005. *Journal of Geophysical Research*, *115*, A07103. https://doi.org/10.1029/2009JA015039

Riley, P., Baker, D., Liu, Y. D., Verronen, P., Singer, H., & Güdel, M. (2018). Extreme space weather events: From cradle to grave. *Space Science Reviews*, *214*(1), 1–24. https://doi.org/10.1007/s11214-017-0456-3

Shi, Y., Zesta, E., Connor, H. K., Su, Y.-J., Sutton, E. K., Huang, C. Y., et al. (2017). High-latitude thermosphere neutral density response to solar wind dynamic pressure enhancement. *Journal of Geophysical Research: Space Physics*, *122*, 11,559–11,578. https://doi.org/10.1002/2017JA023889

Siskind, D. E., Barth, C. A., & Roble, R. G. (1989). The response of thermospheric nitric oxide to an auroral storm: 1. Low and middle latitudes. *Journal of Geophysical Research*, *94*(A12), 16,885–16,898. https://doi.org/10.1029/JA094iA12p16885

Tapley, B. D., Bettadpur, S., Watkins, M., & Reigber, C. (2004). The gravity recovery and climate experiment: Mission overview and early results. *Geophysical Research Letters*, *31*, L09607. https://doi.org/10.1029/2004GL019920

Tóth, G., Sokolov, I. V., Gombosi, T. I., Chesney, D. R., Clauer, C. R., De Zeeuw, D. L., et al. (2005). Space weather modeling framework: A new tool for the space science community. *Journal of Geophysical Research*, *110*, A12226. https://doi.org/10.1029/2005JA011126

Tsurutani, B. T., Gonzalez, W. D., Lakhina, G. S., & Alex, S. (2003). The extreme magnetic storm of 1–2 September 1859. *Journal of Geophysical Research*, *108*(A7), 1268. https://doi.org/10.1029/2002JA009504

Verkhoglyadova, O. P., Tsurutani, B. T., & Mannucci, A. J. (2007). Temporal Development of Dayside TEC Variations During the October 30, 2003 Superstorm: Matching Modeling to Observations. In M. Duldig (Ed.), *Advances in Geosciences* (Vol. 8, pp.69–77). Hackensack, NJ: World Scientific. https://doi.org/10.1142/9789812708939 0004

Zesta, E., & Huang, C. Y. (2016). Satellite orbital drag. In G. V. Khazanov (Ed.), *Space weather fundamentals* (pp. 329–351). Boca Raton, FL: CRC Press.

Zhang, Y., Paxton, J., Gang, L., & Yee, S. (2019). Impact of nitric oxide, solar EUV and particle precipitation on thermospheric density decrease. *Journal of Atmospheric and Solar-Terrestrial Physics*, *182*, 147–154. https://doi.org/10.1016/j.jastp.2018.11.016